JGR Atmospheres

Key Points:

- Precipitation in northeast China cold vortex produces negative upper-level potential vorticity (PV) anomaly that weakens the upper level cold vortex
- Negative PV anomaly produced at the bent-back front is the dominant contributor to the erosion of upper-level high PV in the vortex center
- Lower-level vortex is enhanced by positive PV anomaly from precipitation, and the PV has diurnal variations due to surface heating/cooling

Author Contributions:
Conceptualization: Ziqi Fan, Ming Xue
Data curation: Kefeng Zhu
Formal analysis: Ziqi Fan
Investigation: Ziqi Fan
Methodology: Ziqi Fan
Resources: Kefeng Zhu, Zongting Gao, Shangfeng Li
Software: Ziqi Fan
Supervision: Ming Xue
Validation: Ziqi Fan
Visualization: Ziqi Fan
Writing – original draft: Ziqi Fan
Writing – review & editing: Ziqi Fan, Ming Xue, Kefeng Zhu, Liping Luo

Effects of Precipitation Latent Heating on Structure and Evolution of Northeast China Cold Vortex: A PV Perspective

Ziqi Fan[1], Ming Xue[1,2] , Kefeng Zhu[3], Liping Luo[4], Zongting Gao[5] , and Shangfeng Li[5]

[1]Key Laboratory of Mesoscale Severe Weather, Ministry of Education and School of Atmospheric Sciences, Nanjing University, Nanjing, China, [2]Center for Analysis and Prediction of Storms and School of Meteorology, University of Oklahoma, Norman, OK, USA, [3]CMA Key Laboratory of Transportation Meteorology, Nanjing Joint Institute for Atmospheric Science, Nanjing, China, [4]College of Civil Aviation, Nanjing University of Aeronautics and Astronautics, Nanjing, China, [5]Jilin Provincial Key Laboratory of Changbai Mountain Meteorology & Climate Change, Laboratory of Research for Middle-High Latitude Circulation and East Asian Monsoon, Institute of Meteorological Sciences of Jilin Province, Changchun, China

Abstract Based on potential vorticity (PV) thinking, northeast China cold vortex (NCCV) corresponds to an upper-level high PV anomaly from stratospheric PV downward intrusion. Within a vortex, latent heating from precipitation would produce a vertical dipole of PV anomalies that would affect structures and evolution of the vortex. In this paper, three-dimensional structures and evolution of NCCV and, effects of latent heating from precipitation along bent-back, cold and warm fronts on them are investigated based on convection-allowing simulations for an intense NCCV case during 8–17 June 2012. Trajectory analysis shows that the negative upper-level diabatic PV anomaly from bent-back frontal precipitation, near the vortex center, is the dominant contributor to erosion of high PV in the vortex core region as it is advected in, leading to the weakening of the vortex. The negative PV anomalies along the cold and warm fronts, at the east-to-southeast side of the vortex, are mostly advected downstream away from the NCCV. In the middle troposphere, positive PV anomalies are primarily generated along fronts and the accumulated positive PV anomalies filling the vortex region help to reinforce the low-level cyclonic circulation. The lower-level PV is affected by surface heating and cooling through their effects on static stability, but such effects are periodic and create mainly diurnal variations. The NCCV eventually decays as the upper-level vortex weakens due to significant PV erosion.

Plain Language Summary Northeast China cold vortex (NCCV) is responsible for much of the warm season precipitation in northeast China. Based on convection-allowing simulations of a characteristic case, the distribution and effects of latent heating release from precipitation in bent-back, cold and warm frontal regions on the structures and evolution of potential vorticity (PV) within the NCCV are studied. Negative upper-level PV anomalies generated at the bent-back front are primarily responsible for the filamentation and erosion of high PV in the core of NCCV, leading to the weakening of the vortex. At middle-to-low levels, positive PV anomalies generated reinforce the low-level circulations. However, the lower-level PV exhibits a significant diurnal cycle, which is mainly affected by the surface heating and cooling through reducing static stability at daytime and increasing static stability during night. The overall system eventually decays as the upper-level vortex weakens.

1. Introduction

Cold vortex is a closed cyclonic circulation with a cold core, usually found in the middle to upper troposphere at middle to high latitudes (Hsieh, 1949; Palmén & Newton, 1969). On the middle-to-upper level weather charts, cold vortices usually exhibit themselves as cut-off lows (e.g., Porcù et al., 2007; Xu et al., 2023). Northeastern China extending into the Siberia region is one of the preferred areas for cold vortices in the Northern Hemisphere (Bell & Bosart, 1989; Hu et al., 2010; Nieto et al., 2005). The northeast China cold vortices (NCCVs), usually lasting between a few days to more than 1 week, contribute to much of the local high-impact weathers in the northern China, including heavy precipitation, hailstorms, and even tornados (e.g., Wang et al., 2022; Wei et al., 2023; Xie et al., 2012). C. Zhang et al. (2008) showed that about 55% of hailstorms and 22% of rainstorms in northeast China are caused by NCCVs from April to September in 1979–2005. When an NCCV is

slow-moving or quasi-stationary, the associated precipitation can accumulate over the same region (L. Zhang & Li, 2009), causing severe flooding (Gao & Gao, 2018).

Potential vorticity (PV) is often used to study the structure and evolution of mid-latitude weather systems including cold vortices (e.g., R. Portmann et al., 2018; Rossa et al., 2000) because of its conservation property in the absence of diabatic and frictional processes and invertibility for balanced flows (Hoskins et al., 1985). Understanding physical and dynamical processes in weather systems by analyzing the production/destruction and evolution of PV is part of the so-called PV thinking or PV perspective (Hoskins et al., 1985). In terms of PV, a cold vortex corresponds to a closed region of high PV anomaly that is associated with downward intrusion of stratospheric high PV along isentropic surfaces.

The equation for the PV considering effects of diabatic heating can be expressed as, following Equation 71 of Hoskins et al. (1985):

$$\frac{d\text{PV}}{dt} = \alpha \varsigma_a \frac{\partial \dot{\theta}}{\partial z} \tag{1}$$

PV is defined as

$$\text{PV} = \alpha \, \varsigma_a \frac{\partial \theta}{\partial z} \tag{2}$$

where α is the specific volume of air, ς_a the vertical component of absolute vorticity, θ the potential temperature, $\dot{\theta}$ the diabatic heating rate to potential temperature, and the frictional effect is ignored. From the equation, diabatic heating leads to destruction (production) of PV above (below) the level of maximum heating. Given that the maximum of latent heating from precipitation is generally at the middle to upper troposphere, negative PV anomaly is usually generated at the upper levels, while positive PV anomaly is generated in the lower to middle troposphere. The negative anomaly generated at the upper levels in precipitation regions can be advected into the high PV core of vortex, and through turbulent mixing, would erode the high PV core (Gouget et al., 2000; Wirth, 1995).

Based on the PV perspective, cold vortices decay mainly through two processes: reabsorption back into the high PV stratospheric reservoir (Hoskins et al., 1985; Knippertz & Martin, 2007) or PV erosion at upper levels by diabatic processes (Bourqui, 2006; Lamarque & Hess, 1994; Price & Vaughan, 1993). Raphael Portmann et al. (2021) performed a climatological study on these two ways of decay based on more than 150,000 global cold vortices during 1979–2018, and found that their occurrence frequencies are similar. Fan et al. (2023) classified NCCVs during April to September in 2009–2018 into 5 categories according to the NCCV center locations and found that NCCVs moving southeastward to regions close to the ocean tend to decay via diabatic processes because of heavier precipitation produced, whereas NCCVs moving eastward or northeastward tend to decay through the reabsorption process. Compared to the reabsorption process, the effects of diabatic processes on cold vortex decay are more complicated.

The low-level positive PV anomaly generated by maximum mid-level diabatic heating can help extend the upper-level high PV to lower levels. Surface cooling can also increase near-surface PV. Together with the downward intrusion of stratospheric high PV, a "PV tower" would form (Rossa et al., 2000), which is often associated with extratropical cyclone intensification. Several studies on rapidly deepening extratropical cyclones found such a PV tower at the cyclone center, and examples include the "Presidents' Day Cyclone" (Uccellini et al., 1987; Whitaker et al., 1988), the "Super storm of 1993 (Bosart et al., 1996), and the winter storm "Lothar" (Wernli et al., 2002). In addition, the diabatic positive PV anomaly enhances the low-level cyclonic winds, promotes further poleward advection of warm and moist air from southeast side of cold vortex and contributes to intensification of the surface cyclone and its related winds (Crezee et al., 2017; Davis, 1992).

Previous studies mostly focus on the effect of diabatic PV anomaly on either the weakening of upper-level cold vortex or the intensification of surface cyclone (e.g., Attinger et al., 2019; Harvey et al., 2020). Few studies examine the effects of diabatically generated PV anomalies on the three-dimensional structure and evolution of cold vortex, in the kind of detail that can be revealed by convection-allowing numerical simulations. Such studies on cold vortices in northern China are even more scarce. NCCV is usually accompanied by significant precipitation (Nieto et al., 2005; Zhao & Sun, 2007), and studying the effects of precipitation latent heating on the structure

and evolution of NCCV is important to the understanding and prediction of NCCV and associated weather in northern China. In this study, we focus on the effects of diabatic processes, specifically latent heating from precipitation, on the structure and evolution of NCCV. Another question we want to examine is: precipitation from which region, among those along the cold, warm or bent-back occlusion fronts, is the dominant contributor to upper-level PV erosion.

We choose an intense NCCV in the summer of 2012 as an example to investigate the above issues. This NCCV lasted more than 8 days over northeastern China, and was accompanied by strong cyclonic winds spanning the depth of troposphere and frontal precipitation during mostly the intensification and mature stages of NCCV. We study the case by performing a convection-allowing simulation at 3-km grid spacing, plus a sensitivity simulation in which the diabatic heating and cooling from moist processes are removed by turning off microphysics parameterization. The model prediction is first verified against available observations, and the model output is used to diagnose the effects of diabatically generated PV anomalies. In addition, we briefly examine how low-level PV structures are affected by diabatic heating/cooling from the surface.

The remainder of this article is organized as follows. Section 2 briefly describes the data source and documents the overview of the selected NCCV case. In Section 3, the model configuration used by the numerical simulations is described. Section 4 verifies the simulation against observations and, examines the effects of frontal precipitation and the associated diabatically generated PV anomalies on the three-dimensional structure and evolution of the NCCV. A summary and conclusions are presented in the Section 5.

2. Data Sets and Case Overview

In this study, we use the fifth-generation ECMWF global reanalysis or ERA5 data (Bonavita et al., 2016; Hersbach et al., 2020) to show the synoptic patterns and to provide the initial and boundary conditions of model simulations. The ERA5 is based on a hybrid incremental 4D-Var data assimilation system and contains three-dimensional atmospheric fields at hourly intervals. Pressure level data at 0.25° horizontal resolution is used in this study. Hourly precipitation observations at surface stations from the Chinese Meteorological Administration are used to show the observed precipitation distribution and intensity, and to validate the model simulation.

The intense NCCV that occurred in northeast China from 18 UTC 8 June through 00 UTC 17 June 2012 is chosen for detailed study in this paper. This NCCV intensified from 9 June as it traveled eastward and arrive the Buir Lake at 00 UTC 10 June (the blue line with dots in Figure 1a shows the track of observed vortex center); it started to weaken from then (blue dashed line in Figure 1b) and move southward gradually. Here we define the NCCV center as the geopotential height minimum within the vortex at 500 hPa. From 12 UTC 12 June to 00 UTC 13 June, the vortex center jumped westward (Figure 1a); this is because at 12 UTC 12 June, the vortex became much elongated in the east and west direction with two circulation centers. The western center became stronger than the eastern one during the period, causing the jump of the primary center. Later on, the western center continued to dominate.

At 00 UTC 9 June, the eastern edge of the NCCV at 500 hPa reached the northwestern Heilongjiang Province in northeast China without producing much precipitation (Figure 2a). As the NCCV moved eastward, the southeast part of the NCCV at 500 hPa covered the entire northeast China and, precipitation was present along the cold front and the occluding bend-back front at 12 UTC 9 June (Figure 2b). At this time, strong cold front precipitation, which is in the southeast part of the NCCV, stretched from the Bohai Bay northward to the Heilongjiang Province, and the maximum hourly rainfall was 49.99 mm. In comparison, the precipitation along the bent-back front, which is near the NCCV center, was much weaker and the maximum hourly rainfall was less than 5 mm. Afterward, the NCCV continued to move eastward; at 00 UTC 10 June, the central geopotential height at 500 hPa is reduced from 5411 gpm to 5364 gpm (Figure 1b), and the vortex reached its mature stage with its center located near the Buir Lake (Figure 1a). During the period, the precipitation near the NCCV center along the bent-back front intensified significantly, whereas the precipitation along the cold front weakened greatly (Figure 2d). Over the subsequent 12 hr, the NCCV moved southward slowly while the precipitation along the cold front, especially that at the southernmost end, moved eastward and intensified. Warm frontal precipitation in the east of the NCCV also developed (Figures 2e and 2f). During this period, the NCCV weakened in terms of its center geopotential height at 500 hPa (Figure 1b). From 00 UTC 11 June, the frontal precipitation also weakened significantly, and remaining precipitation was mostly found near the vortex center (Figures 2g and 2h). Moreover, a minor cold
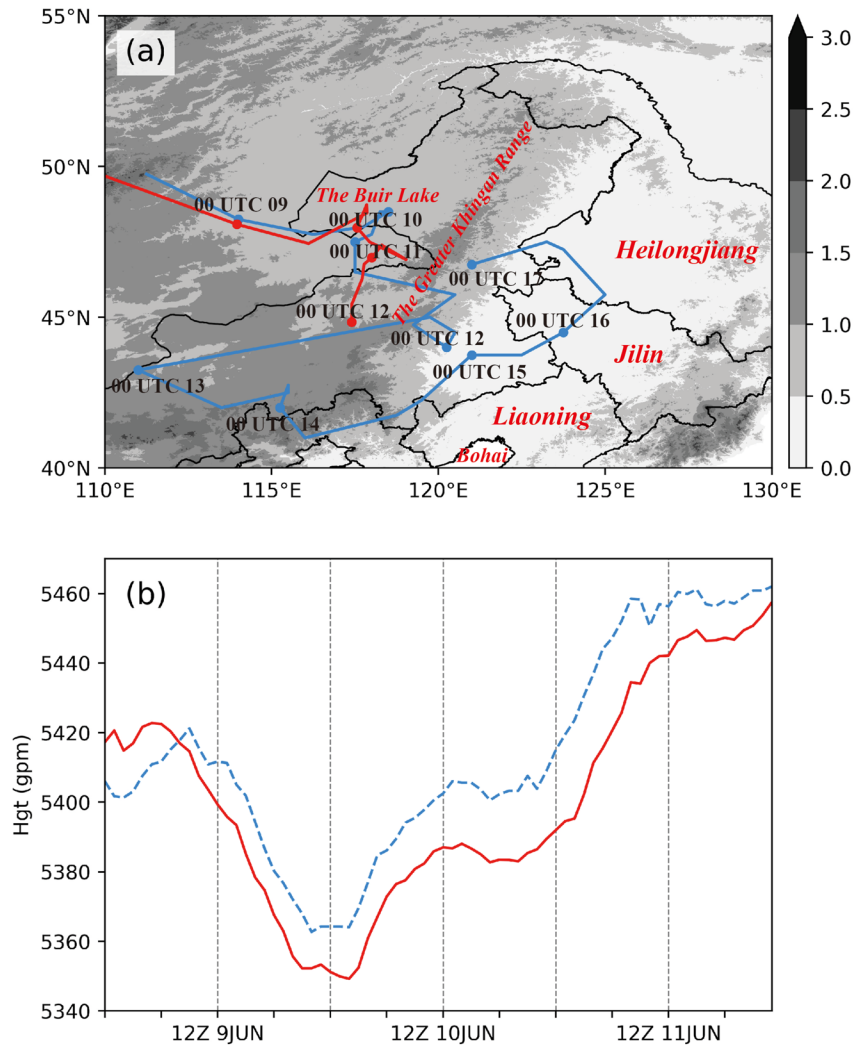
Figure 1. (a) The tracks of the northeast China cold vortice (NCCV) center at 500 hPa at 6-hr intervals from the ERA5 reanalysis data set (blue) during its entire lifespan from 18 UTC 8 June to 00 UTC 17 June 2012 and from the control experiment (red) from 18 UTC 8 June to 00 UTC 12 June 2012. Also shown is terrain elevation in northeast China (shaded, km). (b) Time series of the NCCV central geopotential height at 500 hPa from the ERA5 reanalysis data set (blue dashed line, gpm) and control experiment (red solid line, gpm) at 1-hr intervals from 00 UTC 9 June through 23 UTC 11 June.

vortex with high PV moved southeastward and merged into the NCCV, intensifying the entire system. As shown in Figure 1a, the NCCV center at 500 hPa shifted southwestward by approximately 1,000 km from 00 UTC 12 through 00 UTC 13 June due to the merger of the aforementioned vortex systems.

By 00 UTC 17 June, the NCCV had moved from the southern flank to the eastern flank of the Greater Khingan Range (Figure 1a) and was no longer producing much precipitation. In this study, we will focus on the period from 9 June through 11 June, which covers the development and mature stages, and the first 2 days of the decay stage of the NCCV but before the merger with another vortex; most of the precipitation was produced during this period.

3. Model Configuration of Simulations

The NCCV case of June 2012 is simulated using the Advanced Research version of the Weather Research and Forecast (WRF-ARW) model Version 4.2 (Skamarock et al., 2019) at a 3-km grid spacing. The model is initialized on 1800UTC 8 June 2012 and is run for 78 hr through 00 UTC 12 June 2012. As mentioned earlier, the ERA5 reanalysis datasets at 1-hr intervals are used as the initial condition and boundary conditions. A single model
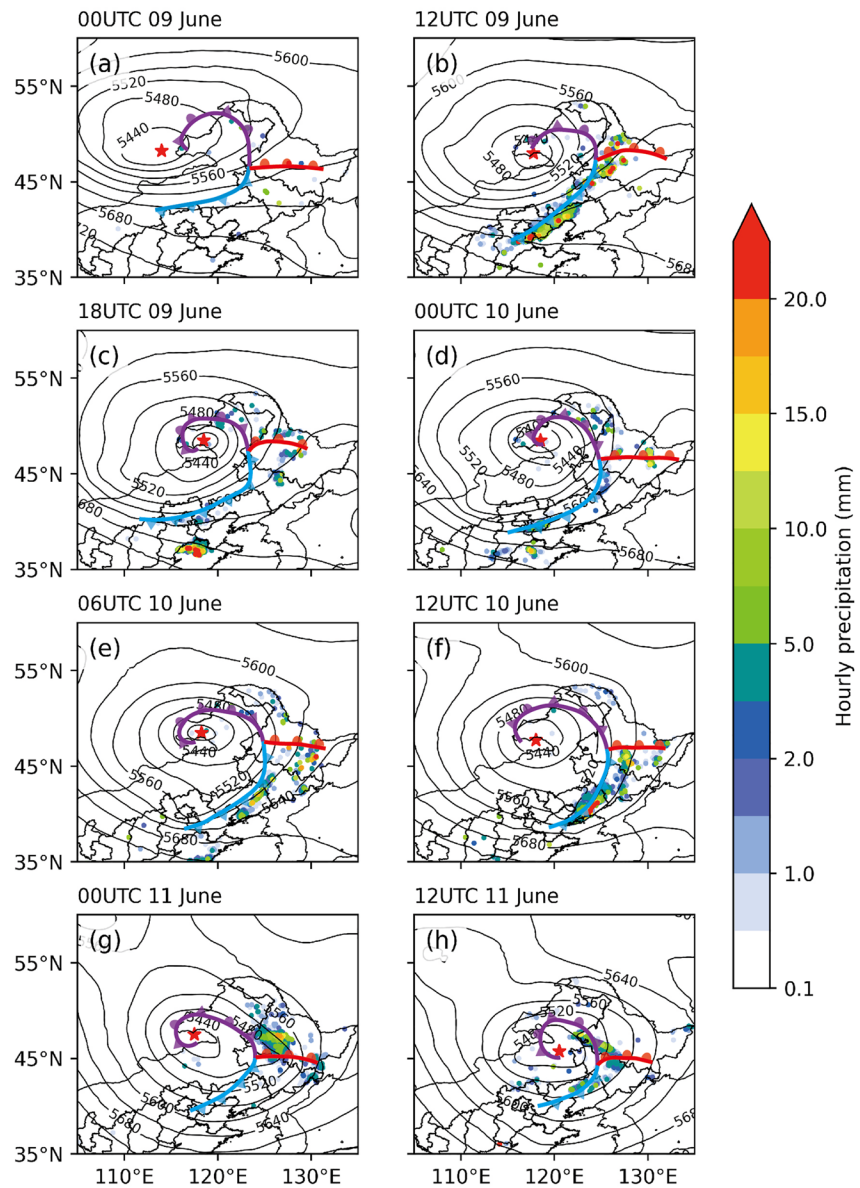
Figure 2. Observed hourly precipitation (dots, mm) at available surface stations (not available outside China) and geopotential height at 500 hPa (contours, gpm) from ERA5 data set. The red star indicates the northeast China cold vortex center at 500 hPa. The cold, warm and occluding bent-back fronts are shown in blue, red and purple frontal symbols, respectively.

domain centered at (47.5°N, 120°E) is used and, the domain has $1,001 \times 1,181$ horizontal grid points and 51 vertical levels. The physics parameterizations applied include the Thompson microphysics scheme (Thompson et al., 2004, 2008), the Mellor-Yamada Nakanishi and Niino 2.5 level (MYNN2.5) planetary boundary layer scheme (Nakanishi & Niino, 2004, 2006), the unified Noah land-surface model (Chen & Dudhia, 2001a, 2001b), and the rapid radiative transfer (rrtmg) short- and long-wave radiation schemes (Mlawer et al., 1997). No cumulus parameterization is used. This experiment is referred to as the control experiment (CNTL, hereafter). To help isolate the effects of diabatic heating from moist processes on the NCCV structure and evolution, we run an additional experiment (called NLH) with the microphysics parameterization turned off throughout the simulation. Model outputs are produced every hour. In addition, the model outputs from 06 UTC 9 June through 00 UTC 11 June 2012 are produced every 5 min to calculate forward trajectories of air parcels discussed in the Section 4.3.1.

Geopotential height at 500 hPa from the control simulation is verified against the ERA5 data, while precipitation from the control simulation is verified against the hourly precipitation observations introduced earlier. This
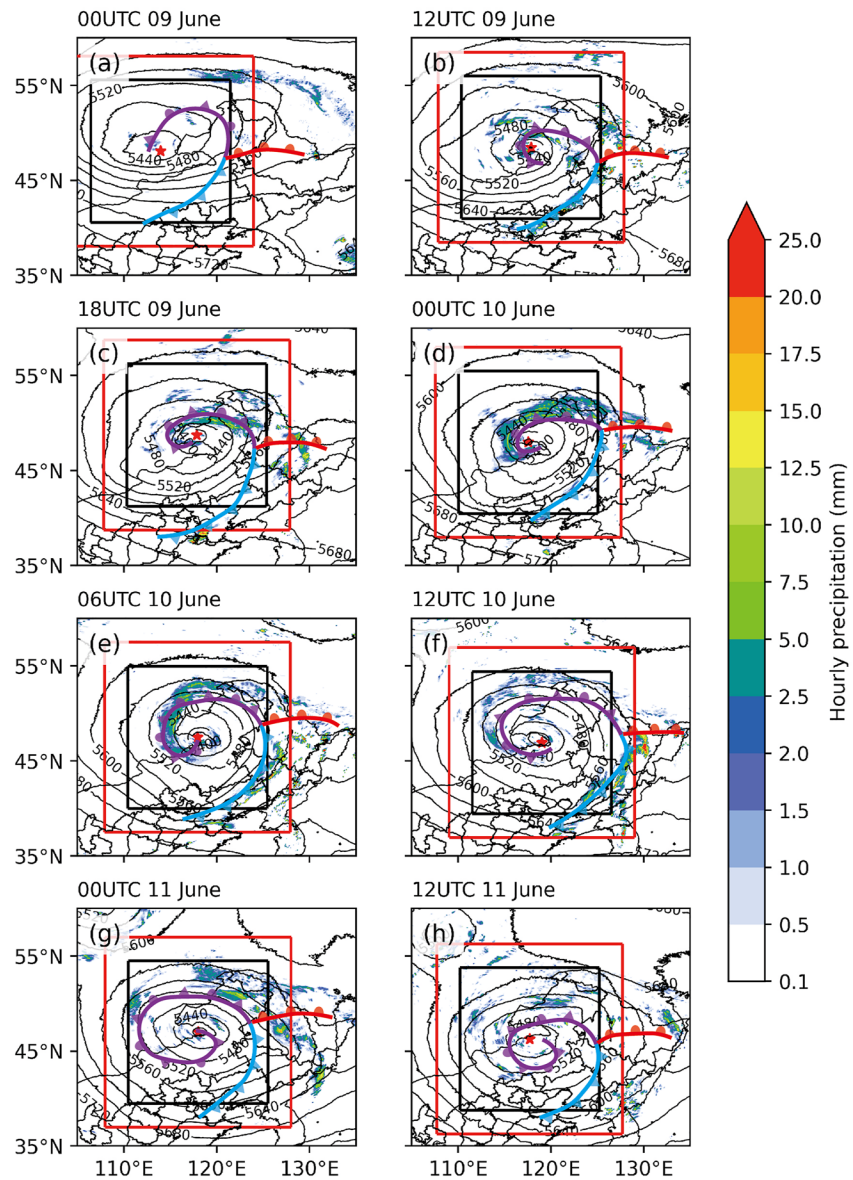
Figure 3. Same as Figure 2, but from the control simulation (CNTL). The black box and red box represent the areas used to do spatial average of potential vorticity and latent heating in Section 4.2, respectively.

observed precipitation data has been used to evaluate realtime precipitation forecasts of the WRF-ARW model at 4-km grid spacing over summer months of 2013 and 2014 in Zhu et al. (2018). Simple quality control procedures were applied, including removal of duplicate sites, time, and space continuity check, and exclusion of abnormal values, as was described in Zhu et al. (2018).

4. Precipitation and Evolution of the Simulated NCCV

4.1. Verification of Control Simulation

The CNTL simulation successfully reproduces the general NCCV patterns in terms of the 500 hPa geopotential height (Figure 3) and the track of vortex center passing through the Greater Khingan Range into northeast China from 9 June to 11 June (the red track with dots in Figure 1a). The general evolution of the simulated intensity from 9 June to 11 June is similar to that observed, although the simulated center is about 20 gpm lower after 08 UTC 9 June (Figure 1b). In addition, CNTL reproduces frontal precipitation distribution similar to the observation, with

the maximum hourly precipitation simulated at 47.24 mm compared to observed 49.99 mm at 12 UTC 10 June. As the simulated 500 hPa geopotential height pattern is much similar to that in ERA5 over the 3 days, we focus on the comparison of precipitation from the CNTL experiment and observations.

At 00 UTC 9 June, the simulated precipitation field is generally similar to that in observations (Figures 3a and 2a), with loosely organized weak precipitation near the vortex center that would become part of the precipitation along the bent-back front. In observations, fragmented precipitation also occurred in the southeast part of the vortex, which is not found in the simulation. In addition, a simulated weak rainfall band located northeast of the vortex is not found in the observations; that region is outside China so our data set does not contain observations there.

By 12 UTC 9 June, the simulated precipitation along the cold front has organized into a strong rain band stretching southwest to northeast across northwest Heilongjiang Province (Figure 3b). It compares favorably with the observations (Figure 2b), although the simulation underpredicts the observed precipitation especially at the south part of the cold front (the area of simulated precipitation above 10 mm is much smaller than that in observations). In addition, weak precipitation along the bent-back front is simulated near the vortex center, slightly heavier than observations. As the vortex intensifies, more precipitation has developed near the Buir Lake along the bent-back front near the vortex center by 18 UTC 9 June (Figure 3c), similar to observations (Figure 2c), although the simulated precipitation is heavier and better organized. Between 18 UTC 9 June and 12 UTC 10 June, the bent-back front spirals further around the vortex center (Figures 3c–3f) and precipitation along the front intensifies and becomes best organized at 00 UTC 10 June (Figure 3d). It maintains its intensity until 06 UTC 10 June when it starts to weaken (Figure 3e). By 12 UTC 11 June, only light precipitation within NCCV is produced in the simulation (Figure 3h), whereas the observed precipitation east of the vortex center is still strong (Figure 2h). Between 12 UTC 9 June and 00 UTC 10 June, the precipitation along the cold (warm) front weakens (intensifies) (Figures 3b–3d), similar to the observations (Figures 2b–2d). By 12 UTC 10 June, the precipitation along the cold front has moved eastward and intensified, due to the availability of richer low-level moisture closer to the coast (Figure 3f), but the precipitation, especially that along the southern part of the cold front, is weaker than that observed (Figure 2f) (maximum of about 10 vs. 25 mm). The precipitation along the warm front has weakened obviously since 06 UTC 10 June (Figure 3e).

In summary, the CNTL experiment reproduces the track (Figure 1a), intensity (Figure 1b) and the 500 hPa geopotential height pattern of the NCCV between 9 June and 11 June (Figure 3), and the distributions and evolution of associated precipitation (Figure 3) reasonably well. However, the simulation underpredicts the hourly accumulated precipitation somewhat. Despite the discrepancies, we believe the general dynamic and physical processes associated with the evolution of the NCCV are captured well enough; and the output of CNTL experiment can be analyzed to study the structure and evolution of the NCCV, as well as the effects of latent heating from precipitation.

4.2. The Evolution of PV and Diabatic PV Anomalies Within the NCCV

To examine the NCCV intensity change in terms of PV, we calculate the mean PV within a $15 \times 15°$ box centered at the cyclonic circulation of the cold vortex at 500 hPa (the black box in Figure 3). Figures 4a and 4b show the evolutions of the mean PV at 850 to 200 hPa from 9 June to 11 June in CNTL and NLH experiments. In general, the mean PV decreases from upper to lower troposphere. In CNTL (Figure 4a), we can see two distinct high PV layers: one at the upper levels above 400 hPa which is connected to the high stratospheric PV reservoir and another at lower levels between 700 and 500 hPa. The latter is clearly diabatically induced as it does not exist in NLH (Figure 4b). The high PV between 400 and 200 hPa corresponds to the region of upper-level NCCV with strong cyclonic circulation.

In CNTL, after an initial decrease, the upper-level PV continually increases from about 08 UTC 9 June through 00 UTC 10 June where higher PV values above 400 hPa extend downward (Figure 4a), suggesting intensification of the upper level cold vortex due to downward intrusion of high stratospheric PV. A similar trend is found in NLH (Figure 4b). Afterward, the high PV area lifts gradually, with less changes occur after 00 UTC 11 June in CNTL. As for the mid-level high PV layer, the intensity increases slightly while the vertical extent expands significantly from 06 UTC 9 June to 02 UTC 10 June. At 02 UTC 10 June, the lower edge of the mid-level high PV reaches down to 750 hPa, descending from the initial $\sim$600 hPa level. The highest mean PV value exceeds 0.8 PVU (1 PVU = $10^{-6} \mathrm{m^2 s^{-1} \, K kg^{-1}}$) by 02 UTC 10 June, which is much higher than the climatological tropospheric values
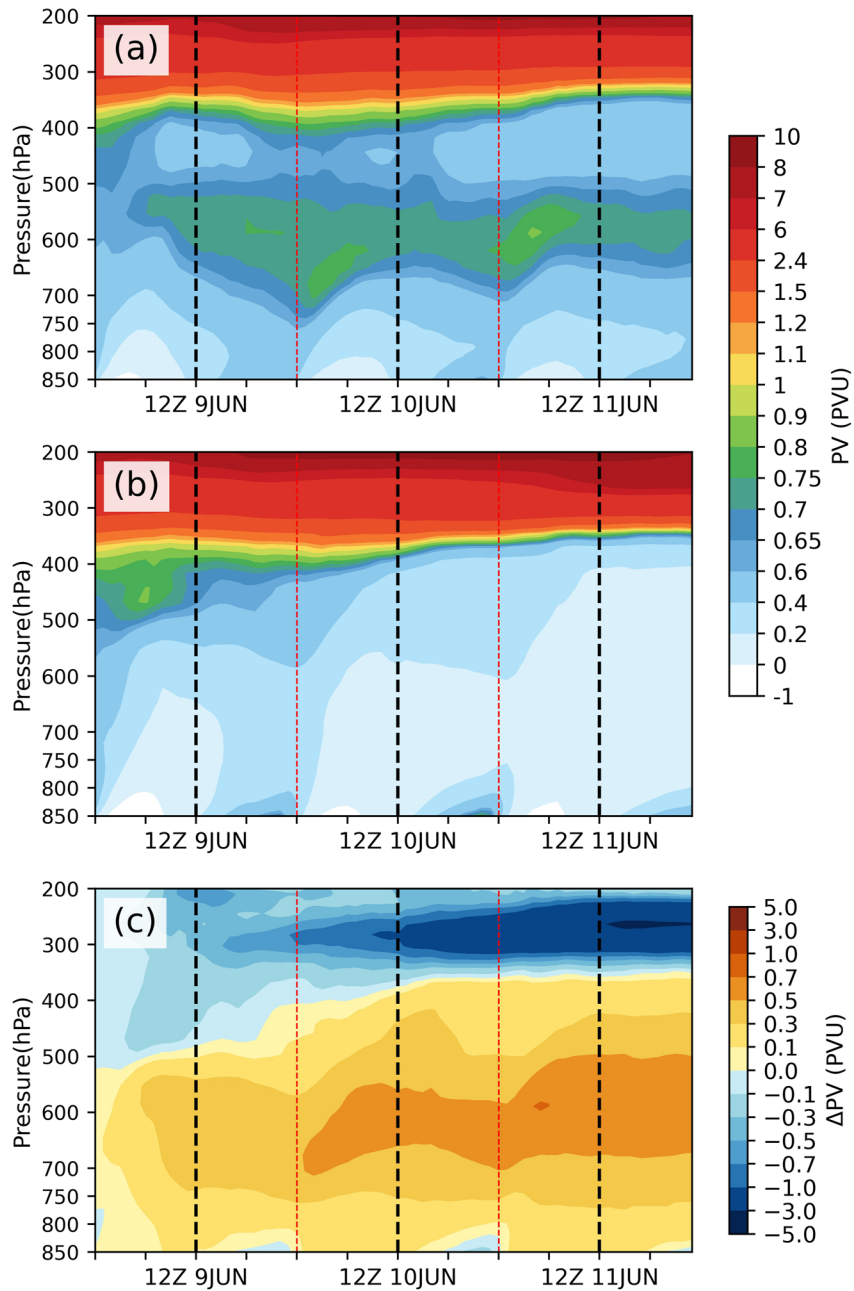
Figure 4. Evolutions of the spatially averaged potential vorticity (PV) over the northeast China cold vortice (within the black box in Figure 3) in (a) CNTL and (b) NLH experiments. (c) Evolution of the PV difference between CNTL and NLH experiments.

of about 0.5 PVU (Čampa & Wernli, 2012). Over the next 12 hr, the lower edge of this high PV layer moves upward around 650 hPa but lowers again for another ~12 hr, and such a cycle repeats over the next 24 hr but at a smaller amplitude. Such cyclic behaviors are apparently related to the diurnal cycle as there are corresponding changes in near surface PV that are associated with diurnal surface cooling and heating.

As precipitation within the NCCV is significant from 9 June to 11 June (Figure 3), the associated latent heating produces diabatic PV anomalies above and below the peak heating level. The diabatic PV anomalies are calculated by subtracting the mean PV of NLH (Figure 4b) from that of CNTL (Figure 4a). As shown in Figure 4c, a vertical dipole of diabatic PV anomalies forms from the upper troposphere down to 850 hPa, with negative PV anomaly of as large as −5 PVUs at the high levels (above 400 hPa) and positive PV anomaly at lower levels
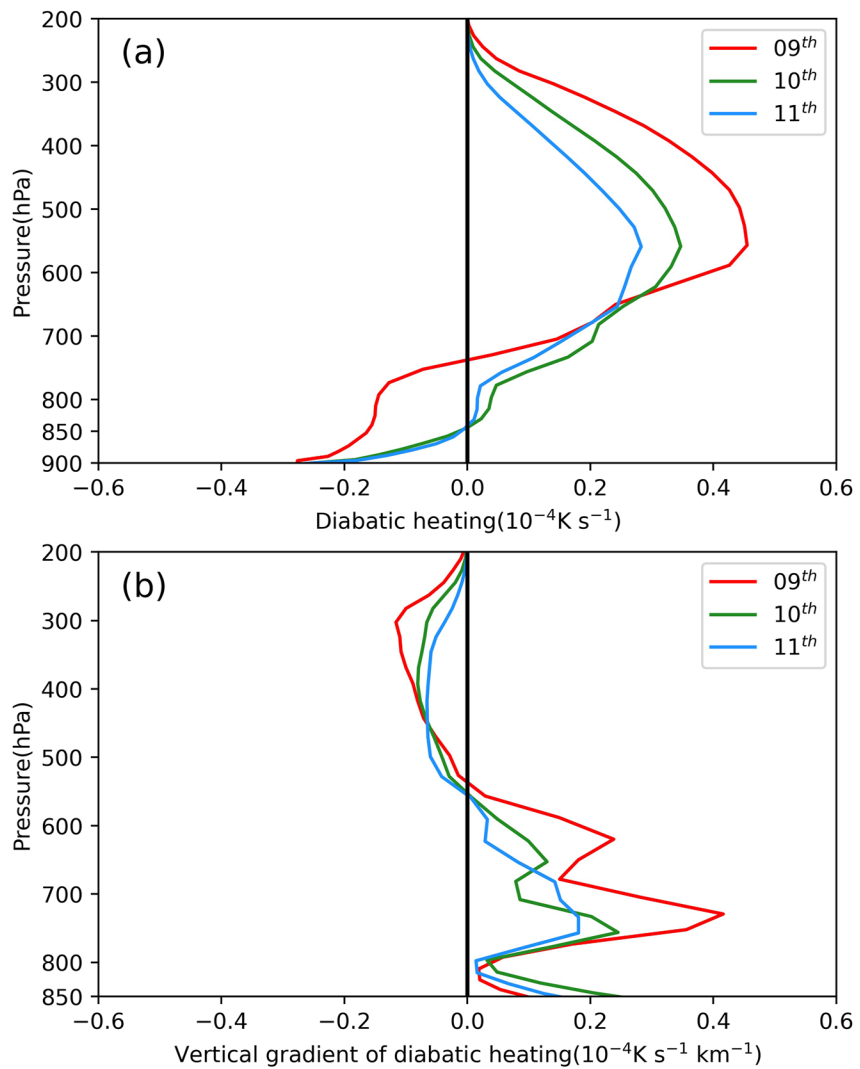
Figure 5. The profiles of (a) mean latent heating and (b) its vertical gradient simulated in CNTL experiment calculated by averaging over 24 hr of 9, 10, 11 June and within a box of $10 \times 10°$ centered on the northeast China cold vortice at 500 hPa (within the red box in Figure 3).

(between 850 and 400–500 hPa), which is similar in pattern to the mid-level high PV layer in CNTL (Figure 4a). As the precipitation continues, the related diabatic PV anomalies accumulate gradually, so that the strength of both negative and positive anomalies increases over the 3 days (Figure 4c). At the upper levels, the strong negative diabatic PV anomaly can significantly erode high PV within the core region of the NCCV and weaken the upper-level vortex, whereas the low-level positive diabatic PV anomaly strengthens the low-level vortex.

From 00 UTC to 18 UTC 9 June, intensities of the two diabatic PV anomalies increase together. Afterward, the high-level negative PV anomaly continues to increase in intensity but shrink in vertical extent. The mid-level positive PV anomaly increases in intensity and extent somewhat, accompanied by diurnal variations. At night, PV near the surface increases due to increase in static stability because of surface cooling. This increase is more in NLH, which should be due to more surface cooling in the absence of cloud cover, thus there are weak negative PV anomalies below 800 hPa before 00 UTC or 08 local standard time (LST).

Figure 5 shows the profiles of mean latent heating and its vertical gradient, that are calculated by averaging over 24 hr for 9, 10 and 11 June, within a box of $20 \times 20°$ centered on the cyclonic circulation of NCCV at 500 hPa (the red box in Figure 3). This box is bigger than that used for calculating the mean PV in Figure 4, in order to cover most of the latent heating from precipitation within the vortex. The average height of the maximum heating

in this NCCV case does not change much (Figure 5a), and remains at about 550 hPa over the 3 days, it reveals that the diabatic PV anomalies concentration height does not change much neither. However, there are significant changes in the intensity and vertical distribution of the heating. On 9 June, more heating is located at higher levels and there is weakening and lowering of heating over the next 2 days. The decrease (increase) in PV above (below) the level of peak heating depends on the vertical gradient of the heating profile (see also Equation 1). During 9 June to 11 June, an obvious vertical dipole of latent heating gradient is shown (Figure 5b), with negative (positive) gradients above (below) 550 hPa, the level of maximum latent heating. The upper-level maximum heating gradient is at about 300–350 hPa in the 3 days, negative PV anomaly is continuously produced at those levels (Figure 4c). At the lower levels, there are more variations in the heating gradients, there are therefore more variations in the production of low-level positive PV anomaly (Figure 4c). The positive gradient at the surface associated with night-time cooling also creates positive PV in the boundary layer.

4.3. The Effects of Latent Heating From Precipitation on Three-Dimensional Structure of NCCV

In this section, we examine in more detail how the diabatically generated PV and its spatial distribution affect the three-dimensional structures of NCCV at different levels. Fields on the 325 K isentropic surface, at the 600 hPa barometric surface and mean fields in the 800–850 hPa layer, are chosen to reveal the structures of NCCV in the upper, middle and lower troposphere, respectively.

4.3.1. Changes in Upper Tropospheric Structures

Due to the conservation property of PV under adiabatic and frictionless conditions, advection dominates the spatial change in PV within the NCCV on isentropic surfaces away from regions of significant precipitation. The height contours in Figure 6 show that the 325 K isentropic surface slopes downward from north to south, the height at 35°N is about 7 km (~400 hPa), which is still above the ~550 hPa peak heating level (Figure 5a), thus negative diabatic PV anomaly would be produced at this level. As shown in Figures 6a and 6b, an elliptical region with PV above 4 PVU marks the vortex region while the yellow area with PV above 8 PVU represents the core region of vortex.

At 00 UTC 9 June (Figures 6a and 6b), a narrow tongue of PV blow 4 PVU is found on the north side of the vortex in both experiments, separating the high PV in the vortex from a strip of high PV to its north. By 12 UTC 9 June, much more differences develop between CNTL and NLH (Figures 6c and 6d). A region of low PV below 2 PVU is found at the southeast edge of the vortex that is being advected northward in CNTL (Figure 6c). Such a low PV region is much weaker and smaller in NLH (Figure 6d). By 06 UTC 10 June, PV below 2 PVU has been advected to wrap around the north and northwest sides of the vortex in CNTL (Figure 6e) and hence significantly reduces the extent of high PV in the vortex. In NLH (Figure 6f), the low PV remains on the east side of the vortex. After that, the low PV tongue in CNTL continues to be advected toward the high PV core region. There are many detailed fine-scale structures in the PV, corresponding to filamentation of both high and low values. The PV filaments are advected further southward by the strong cyclonic flow and stretched thinner. With the help of turbulence, the high and low PV filaments are mixed together (Appenzeller et al., 1996; R. Portmann et al., 2018; Wirth et al., 1997), causing erosion of high PV in the core region, and weakening of the vortex.

By 18 UTC 11 June (Figure 6g), even lower PV (blow 1 PVU) has reached the northwest side of the vortex, and is almost connected with the low PV further west, isolating the high PV within the NCCV core region. In contrast, there is no erosion by negative PV anomaly generated by latent heating in NLH, so the high PV within the vortex and associated vortex circulation are much stronger at 18 UTC 11 June (Figure 6h). The vortex in NLH at 18 UTC (Figure 6h) is actually stronger than earlier times, which may be due to further intrusion of stratospheric PV into the vortex. This suggests even more effect of the latent heating in reducing the intensity of the vortex.

Another important question to ask is: what precipitation, in which part of the vortex, along which front, is most responsible for the upper-level PV erosion in the vortex core region. According to impermeability theorem of PV (Haynes & McIntyre, 1990; Schneider et al., 2003), air parcels with some PV, named PV substances, can only move along not through the isentropic surfaces and is conserved along their trajectories. Thus, to answer this question, forward Lagrangian trajectories are calculated for a number of air parcels starting in the regions of PV less than 1 PVU near or within the precipitation region along the bent-back, warm and cold fronts, respectively (Figure 7). The low PV values in these regions correspond to the strong negative diabatic PV anomalies. Here we assume that the PV anomalies will be advected mostly along the isentropic surfaces, and are more or less
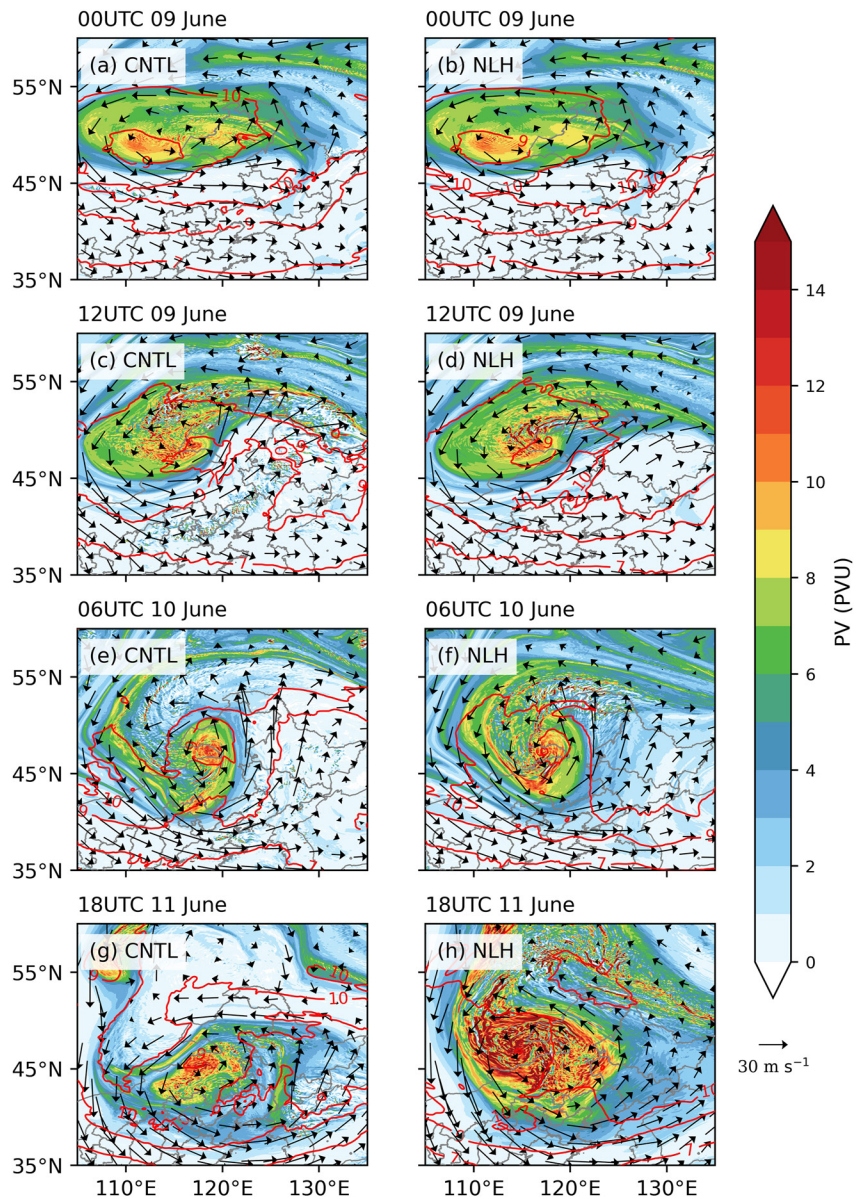
Figure 6. Potential vorticity (shaded, PVU), height (red contours, km) and horizontal wind vectors on the 325 K isentropic surface simulated by the (a, c, e, g) CNTL and (b, d, f, h) NLH experiments at different times shown in the plots.

conserved outside of the precipitation regions. The trajectories are initialized on the 325 K isentropic surface in the low PV regions, from 06 UTC 9 June through 06 UTC 10 June at 6-hr intervals, a period when precipitation is significant (cf. Figure 3). The trajectories are integrated to 00 UTC 11 June using the CNTL experiment output at 5-min intervals, using the fourth-order Runge-Kutta scheme, as in Xu et al. (2017).

We can see that the negative diabatic PV anomalies generated from the bent-back front precipitation and the precipitation in the vortex core region (can also be regarded as part of the spiraling bent-back front) are the main contributors to the erosion of the vortex (Figures 7a–7f). As shown in Figures 7a and 7b, the parcels with negative diabatic PV anomalies, initialized north of the vortex at 06 UTC and 12 UTC 9 June, move southward and cut off the outer edge of high PV from the vortex to cause significant PV filamentation (Figures 7c and 7d). Afterward, these parcels with low PV spiral around the core region (Figure 7e), and push the high PV filaments away from the core region (Figure 7f). From 18 UTC 9 June through 06 UTC 10 June (Figures 7c–7e), the bent-back front precipitation is much stronger and much closer to the vortex core region than before, and the associated
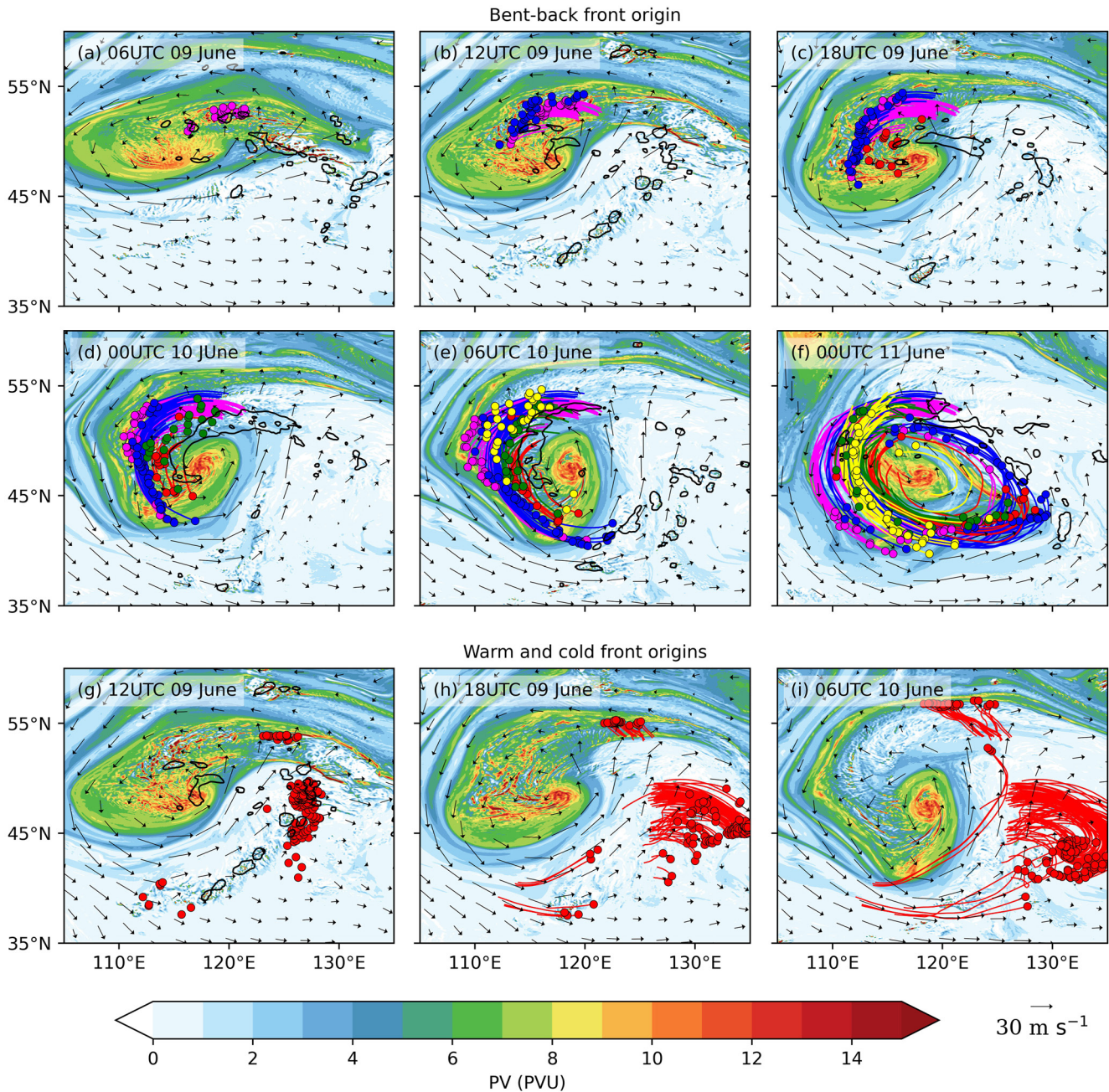
Figure 7. Forward-trajectories of air parcels initialized in regions of potential vorticity (PV) < 1 PVU associated with diabatic negative PV anomaly, from 06 UTC 9 June through 00 UTC 11 June 2012. The first and second rows show the PV (shaded, PVU) and horizontal wind vectors on the 325 K isentropic surface from CNTL experiment, and trajectories (color lines) initialized in the region at 325 K isentropic surface near or within precipitation along the bent-back front. Only those trajectories that end above the 325 K isentropic surface at 00 UTC 11 June and remain above 6 km from the initialization time to 00 UTC 11 June are shown (as they can contribute to the erosion of upper level PV). The black contours represent the areas where the hourly precipitation is above 2 mm. The colored dots at the end of trajectories represent the locations of parcels at the time of plotted fields while the colored dots not associated with trajectories are locations of the parcels initialized at the time of the plotted fields (the subsequent trajectories will be shown in the following panels). The third row is same as the first and second rows, but for trajectories initialized at 12 UTC 09 June along the warm and cold fronts.

negative diabatic PV anomalies are generated just next to the core region. Afterward, as the bent-back front precipitation weakens, the weakening of the upper level vortex slows but the vortex eventually dissipates.

The negative PV anomaly originating from cold frontal precipitation is produced on the south and east side of the vortex which is further away from the vortex center. Most of these parcels move downstream with anticyclonic

flow curvatures so they do not directly affect the core vortex (Figures 7g–7i). For parcels originating from the warm front located on the northeast sides of the vortex (Figure 7g), most move northward outside of the vortex (Figures 7h and 7i), and therefore do not directly contribute to the PV erosion and weakening of the vortex either. Hence, the diabatic negative PV anomaly from bent-back front is the dominant contributor to the erosion of high PV within NCCV core region and affects the vortex intensity change most, even though precipitation at the cold and warm fronts is often more intense.

4.3.2. Changes in Middle and Lower Tropospheric Structures

By comparing to PV fields between CNTL and NLH at 600 hPa, we can see clearly the positive PV generated by precipitation heating that peaks above this level. At 00 UTC 9 June, the main differences are found along a precipitation band in the northeast quadrant of the plotted domain and near the vortex center (cf., Figure 3a) where PV exceeds 2 PVU with many small-scale structures due to precipitation (Figures 8a and 8b). By 12 UTC 9 June, a clear band of high PV is found along the cold front in CNTL (Figure 8c) where significant precipitation is present (cf., Figure 3b). High PV values are also found along the bent-back front and near the vortex center in CNTL (Figure 8c) but not in NLH (Figure 8d).

As time goes on, high PV generated diabatically earlier is advected by the vortex circulation while new PV is generated in the precipitation region, resulting in expansion of the high PV values. By 12 UTC 10 June (Figure 8e), the areal coverage of high PV is the most extensive, with high PV found along the eastward-progressing cold front and the spiraling bent-back front (cf., Figure 3f), as well as on the west side and in the core region of the vortex. In comparison, high PV values found earlier in NLH are decreased (Figure 8f), likely due to diffusion. Given the much-increased PV in CNTL, the vortex circulation is much stronger, as seen in the areal coverage of >15 ms^{-1} wind speed (Figure 8e vs. Figure 8f). The stronger circulation also enhances the spiraling advection of the generated positive PV into the vortex core region, and increase the PV there. While the mid-to-low-level cyclonic vortex strengthens in response to diabatic heating, precipitation is also generally enhanced.

After 12 UTC 10 June, the cold front precipitation is pushed eastward while those along the warm front and bent-back front start to weaken (cf., Figures 3g and 3h). Correspondingly, less new positive PV is generated and the vortex at the 600 hPa becomes somewhat weaker (Figure 8e vs. Figure 8g). The latter may be a response to the weakening of upper-level cold vortex.

Earlier, Figures 4a and 4b show that the mean PV below 750 hPa in both experiments exhibits a clear diurnal variation, with minimum PV at around 12 UTC or 20 LST and maximum before 00 UTC or 08 LST. The amplitude of diurnal variation in CNTL is smaller than that in NLH. The PV anomaly (Figure 4c), or the difference of the mean PV between CNTL and NLH, is positive at 12 UTC and negative before 00 UTC below 800 hPa, that is, the lower-level PV decreases (increases) less in CNTL in daytime (nighttime) than in NLH. Since the differences are more significant in the 800–850 hPa layer, we examine the diurnal variations of mean PV in this layer next.

In NLH (Figure 9), at 12 UTC or 20 LST of the 3 days, most of the PV in the layer is close to 0.25 PVU and few values are above 1.2 PVU, while at 00 UTC or 08 LST, many PV values are above 0.75 PVU especially within the core region of the vortex. Figure 4b shows that high PV values are largest at night at these levels; this is due to the increase in low-level static stability by surface radiative cooling.

Another standout feature of the low-level PV in NLH is the high positive PV bands reaching several PVUs along the cold and bent-back fronts before 00 UTC (08 LST), but they disappear in daytime. The 9 June is selected as an example, when the high PV band along the fronts, especially the cold front, is significant. Since PV is the product of static stability and vorticity (see also Equation 2), PV will be very small if one of them is nearly zero. As seen in the vertical cross sections perpendicular to the cold front (Figure 10), changes in the vertical distribution of potential temperature follow the diurnal cycles of surface heating and cooling. Because of the surface heating and boundary layer turbulent mixing in daytime (Figures 10a and 10b), the low-level potential temperature increases gradually while the top of the mixed layer rises from 850 hPa to 800 hPa or even 700 hPa from 00 UTC through 06 UTC. The nearly zero vertical gradient of potential temperature in the mixed boundary layer significantly reduces PV, causing the disappearance of the high PV bands.

After the sunset (Figures 10c and 10d), surface cooling sets in, the low-level potential temperature decreases from >301 K (307 K) at cold (warm) side of the cold front to 295 K (297 K), starting from near surface upward to 825 hPa or even 800 hPa from 06 UTC to 18 UTC. The difference between 800 and 850 hPa increases from zero
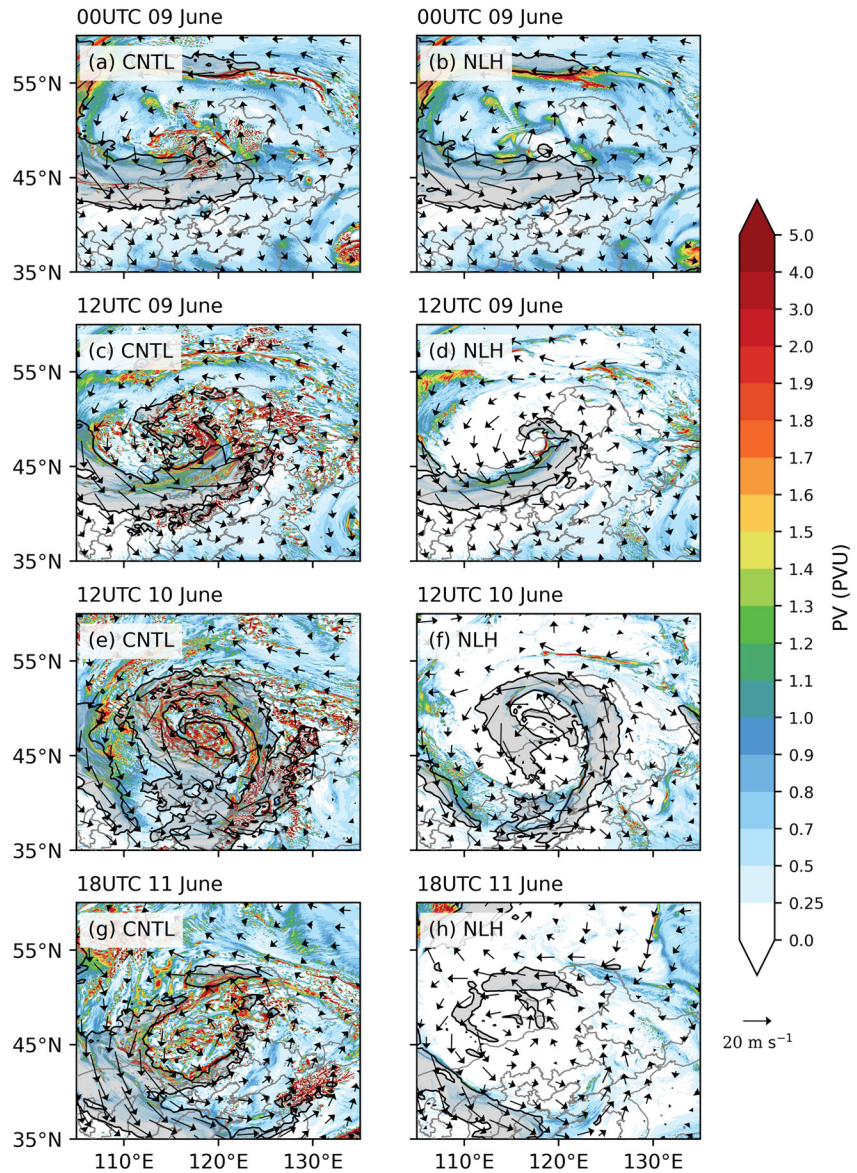
Figure 8. Potential vorticity (color shaded, PVU) and horizontal wind vectors at 600 hPa from (a, c, e, g) CNTL and (b, d, f, h) NLH experiments. The translucent gray shading enclosed by black contours represents the areas where the horizontal wind speed is above 15 ms⁻¹.

to 5 K at the cold front. The significantly increase in static stability increases low-level PV. Meanwhile, significant vertical vorticity along the cold front leads to high PV bands along the front at night.

Within CNTL experiment, the above processes also exist, although the surface cooling is somewhat damped by nighttime cloud cover, resulting in weaker nighttime enhancement of near-surface PV (cf., Figure 4a). Thus, the PV anomaly below 800 hPa shown in Figure 4c is negative before 00 UTC. Since the vertical gradient of latent heating at 800–850 hPa is positive (cf. Figure 5b), there is positive PV anomaly generated by precipitation in CNTL, its PV values at 800–850 hPa (Figure 11) are clearly higher than those in NLH (Figure 9).

5. Summary and Conclusions

In this study, a detailed analysis of the effects of latent heating from precipitation on the three-dimensional structures and evolution of a NCCV (northeast China cold vortex) is performed based on 3-km convection-allowing simulations with and without the precipitation processes. The case is an intense NCCV that occurred from 18
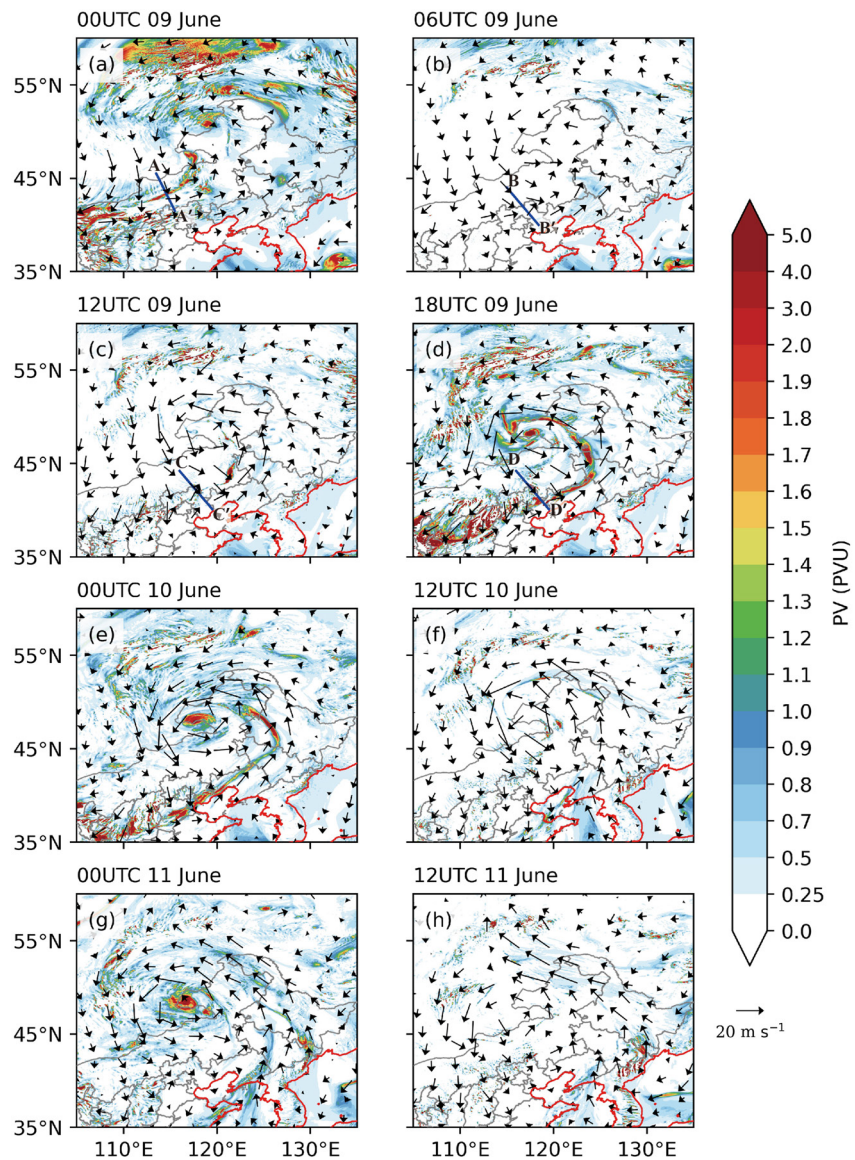
Figure 9. The layer mean potential vorticity (shaded, PVU) and horizontal wind vectors averaged between 800 and 850 hPa simulated by NLH experiment. The coastline is in red. The dark blue line in (a–d) indicate the location of the vertical cross section presented in Figure 10.

UTC 8 June through 00 UTC 17 June 2012 in northeast China. In this study, we focus on a 3-day period from 9 June to 11 June 2012 when the NCCV developed, reached its mature stage, and started to weaken. The PV perspective is adopted to investigate the cold vortex structure and the effects of diabatic heating due to precipitation on its structure and evolution.

In the control simulation over the 3-day period, a vertical dipole of diabatically-generated PV anomalies (calculated as the difference between two simulations with and without latent heating processes associated with precipitation) within the NCCV forms that spans the most of the troposphere due to the latent heating from primarily frontal precipitation. Negative PV anomaly is found at high levels (above 400 hPa) and positive PV anomaly is at middle to lower levels (between 850 and 400–500 hPa). The upper-level negative anomaly is concentrated within a more limited depth of about 200 hPa whereas the lower-level positive anomaly below the level of maximum heating is deeper that spans a layer of over 400 hPa.

In the upper troposphere, the negative diabatic PV anomalies from precipitation along the bent-back front are found to be the dominant contributor to the reduction of high PV in the core region of NCCV, they are advected
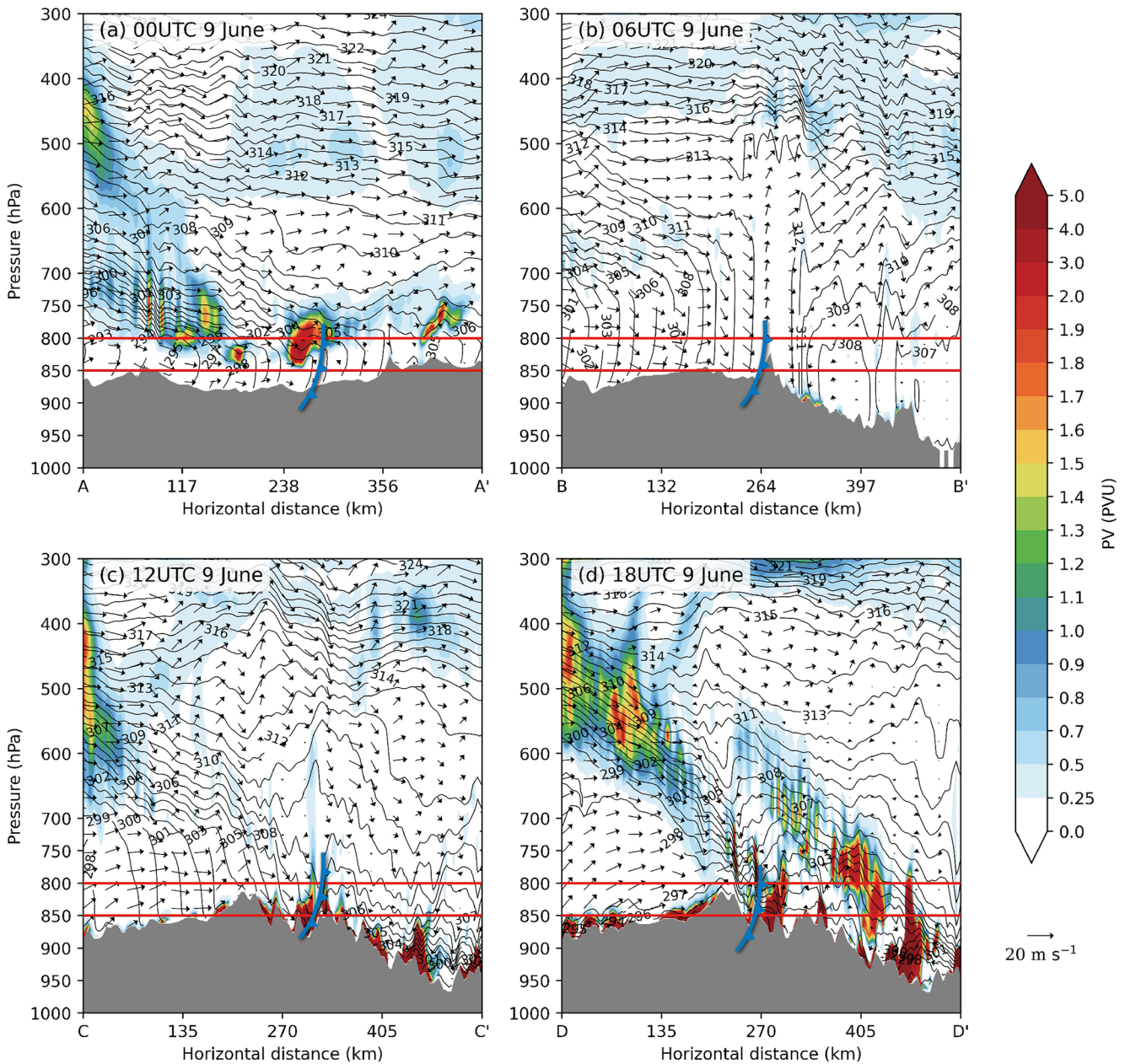
Figure 10. Vertical cross sections of potential vorticity (shaded, PVU), wind vectors and potential temperature (contours, K) along the lines (a) $A-A'$, (b) $B-B'$, (c) $C-C'$, and (d) $D-D'$ on 9 June 2012 shown in Figures 9a–9d. The cold front is shown in blue frontal symbol. The region within the two red lines demonstrate the 800–850 hPa layer.

by the vortex circulation in a spiral pattern toward the vortex core and erode the high PV there. The processes are summarized in the conceptual illustration in Figure 12. The figure shows the evolution of the NCCV in terms of PV subjecting to the effects of negative diabatic PV anomalies from the bent-back frontal precipitation in a higher-level isentropic surface. In the early stage of a developed NCCV, the vortex has an elliptic shape filled with high PV (Figure 12a). When precipitation develops along the occluding bent-back front, a wedge of negative PV anomaly produced by latent heating of precipitation is generated at the northeast side of vortex (Figure 12b), and is advected by the cyclonic circulation to the north side of vortex where additional negative PV anomaly is generated as the bent-back front extends further westward (Figure 12c). Over the next 12 hr, the low PV associated with negative anomalies are further advected around the vortex core to reach its southwest side while additional negative PV anomalies are generated by precipitation along the way (Figure 12d). Such processes continue over
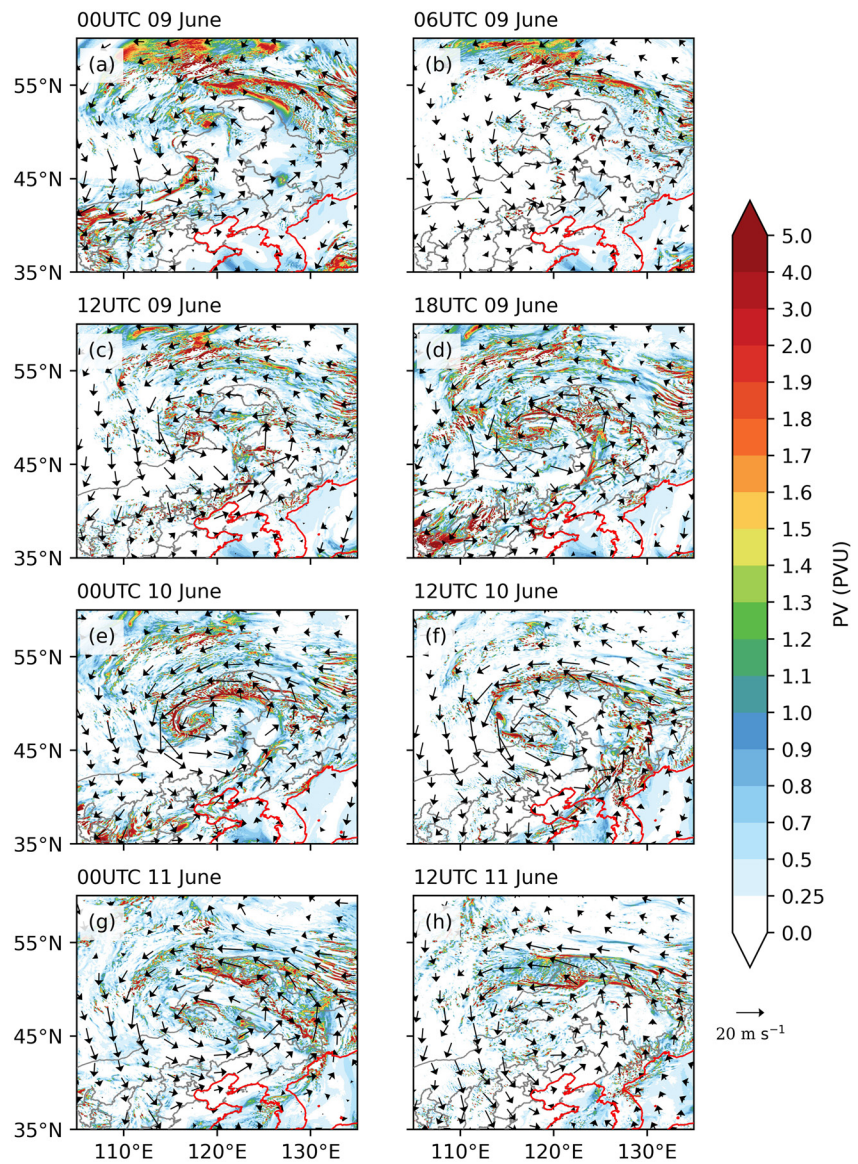
Figure 11. Same as Figure 9, but from the CNTL experiment.

the next 24 hr, with the areas of increasingly lower PV expanding and completely enveloping the much reduced the core region of vortex with high PV (Figures 12e and 12f). As the processes proceed, the high PV along the outer edge of the vortex gets more and more "peeled off" and separated from the inner core region, and the high PV becomes long, stretched filaments that are gradually diffused by mixing. The low PV gets (often less than 1 PVU) progressively closer to the center of the vortex, significantly eroding the high PV there (Figure 12f), causing the eventual demise of the upper-level cold vortex.

Different from those at the bent-back front, the upper-level negative PV anomalies generated at the cold and warm fronts are mostly advected downstream by anti-cyclonically curved circulations and therefore do not contribute much to the weakening of the cold vortex, even though their associated precipitation is often stronger.

In the middle troposphere (∼600 hPa) below the level of maximum latent heating, higher PV values are found near the regions of frontal precipitation. Positive PV anomalies generated by the latent heating from precipitation are advected to the core region of vortex by the vortex circulation at those levels, resulting in expansion of the areal coverage of high PV and intensification of middle level (as well as lower level) vortex circulation. The stronger circulation also enhances the advection of the positive PV anomalies toward the core region of the
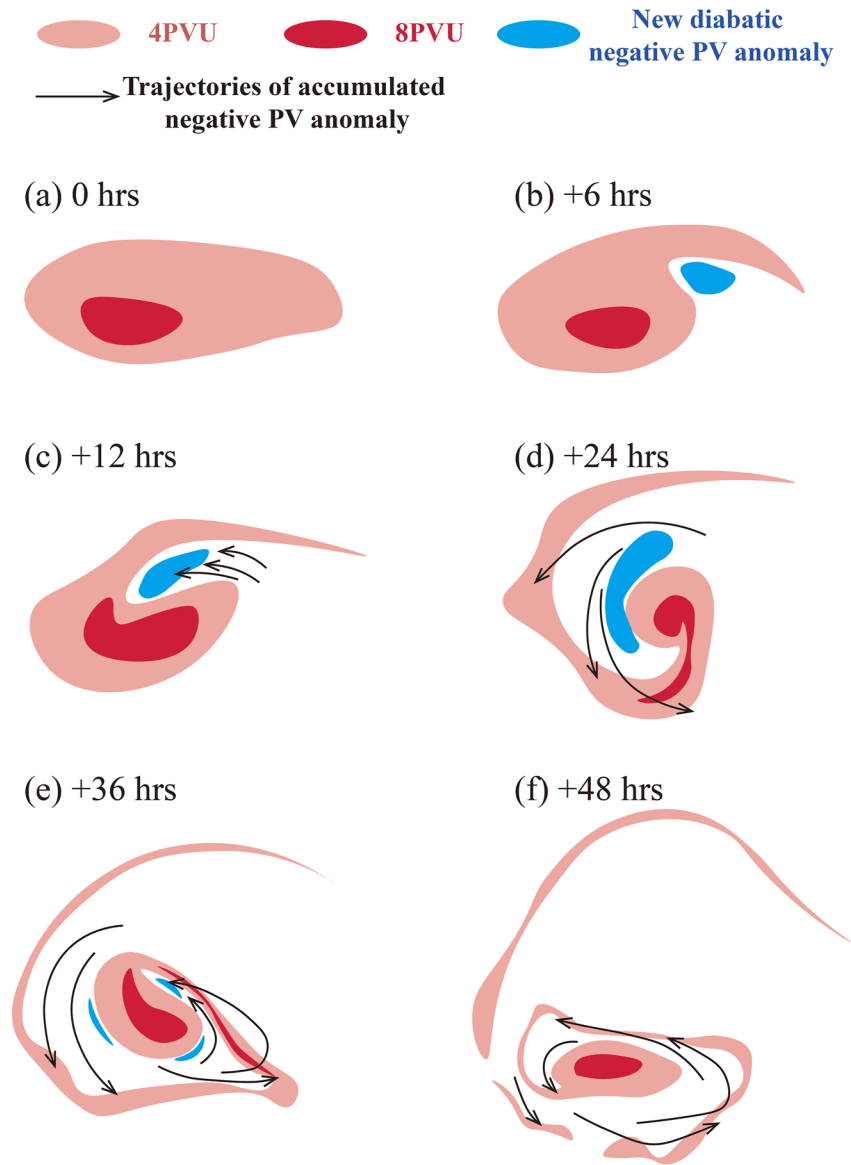
Figure 12. Schematic evolution mechanisms of Northeast China cold vortex (NCCV) on high isentropic surface. The pink and dark red shading represent the areas where the potential vorticity (PV) is above 4 PVU and 8 PVU, which also represents the outer edge and core region of the vortex, respectively. The blue shading represents the negative diabatic PV anomalies newly generated from the bent-back frontal precipitation, while the black arrows represent the trajectories of the accumulated negative PV anomalies.

vortex. The intensification of the middle and lower-level vortex tends to enhance frontal precipitation which in turn would cause the eventual demise of upper-level cold vortex.

At the lower levels (800–850 hPa), the evolution of PV exhibits clear diurnal variations, primarily due to surface heating and cooling effects on static stability. At night, surface cooling significantly increases low-level static stability, creating high PV bands along fronts that is more prominent when precipitation is suppressed in the model. During the day, the development of mixed boundary layer with weak static stability destroys the high PV bands. In the presence of significant frontal precipitation and the associated cloud cover, both night time cooling and day time heating on the surface are damped, so that the diurnal variations in low-level PV are much weaker.

In summary, while NCCV is an important precipitation-producing weather system in northern China, the latent heating from precipitation within NCCV is also an important cause for its demise. The NCCV is primary an

upper-level cold vortex, typically containing high PV sourced from the stratosphere that intrudes into the troposphere. The high upper-level PV helps induce strong low-level cyclonic circulations and associated fully developed fronts. The frontal precipitation with latent heating peaking at the mid-to-upper levels creates negative PV anomalies at upper levels and positive PV anomalies at lower levels, leading to a general lowering of the center of weight of high PV. Besides, the positive PV anomaly at low levels can help to produce a deep PV tower that can lead to explosive development of cyclone in certain situations (Lim & Simmonds, 2002; Pang & Fu, 2017; Wernli et al., 2002). The enhanced low-level circulation also induces stronger northward water vapor advection for more precipitation. Eventually, precipitation leads to the demise of the upper-level cold vortex.

Finally, we believe the main conclusions obtained in this paper are representative of typical cold vortices in northern China. Still, we want to point out that this study is based on a single NCCV case, and more cases should be studied to test the generality of the results obtained.

Data Availability Statement

All data used for analysis and analytical model development are available in the public domain. The evolution of the NCCV case in this study was analyzed using ERA5 reanalysis data from 8 June to 17 June 2012 (available at https://doi.org/10.24381/cds.bd0915c6; Hersbach et al., 2020). The NCCV in this study was simulated by the WRF model v4.2 (Skamarock et al., 2019). The initial and lateral boundary conditions for the WRF model were provided by ERA5 reanalysis data from 8 June to 12 June 2012. The hourly precipitation observation data is available at National Meteorological Information Center of the China Meteorological Administration via https://data.cma.cn/data/. The model outputs used in this paper are available at (Fan, 2023).

References

Appenzeller, C., Davies, H. C., & Norton, W. A. (1996). Fragmentation of stratospheric intrusions. *Journal of Geophysical Research*, *101*(D1), 1435–1456. https://doi.org/10.1029/95JD02674

Attinger, R., Spreitzer, E., Boettcher, M., Forbes, R., Wernli, H., & Joos, H. (2019). Quantifying the role of individual diabatic processes for the formation of PV anomalies in a North Pacific cyclone. *Quarterly Journal of the Royal Meteorological Society*, *145*(723), 2454–2476. https://doi.org/10.1002/qj.3573

Bell, G. D., & Bosart, L. F. (1989). A 15-year climatology of northern hemisphere 500 mb closed cyclone and anticyclone centers. *Monthly Weather Review*, *117*(10), 2142–2164. https://doi.org/10.1175/1520-0493(1989)117<2142:AYCONH>2.0.CO;2

Bonavita, M., Hólm, E., Isaksen, L., & Fisher, M. (2016). The evolution of the ECMWF hybrid data assimilation system. *Quarterly Journal of the Royal Meteorological Society*, *142*(694), 287–303. https://doi.org/10.1002/qj.2652

Bosart, L. F., Hakim, G. J., Tyle, K. R., Bedrick, M. A., Bracken, W. E., Dickinson, M. J., & Schultz, D. M. (1996). Large-scale antecedent conditions associated with the 12–14 March 1993 cyclone ("Superstorm '93") over eastern North America. *Monthly Weather Review*, *124*(9), 1865–1891. https://doi.org/10.1175/1520-0493(1996)124<1865:LSACAW>2.0.CO;2

Bourqui, M. S. (2006). Stratosphere-troposphere exchange from the Lagrangian perspective: A case study and method sensitivities. *Atmospheric Chemistry and Physics*, *6*(9), 2651–2670. https://doi.org/10.5194/acp-6-2651-2006

Čampa, J., & Wernli, H. (2012). A PV perspective on the vertical structure of mature midlatitude cyclones in the northern hemisphere. *Journal of the Atmospheric Sciences*, *69*(2), 725–740. https://doi.org/10.1175/JAS-D-11-050.1

Chen, F., & Dudhia, J. (2001a). Coupling an advanced land surface–hydrology model with the Penn state–NCAR MM5 modeling system. Part I: Model implementation and sensitivity. *Monthly Weather Review*, *129*(4), 569–585. https://doi.org/10.1175/1520-0493(2001)129<0569:CAALSH>2.0.CO;2

Chen, F., & Dudhia, J. (2001b). Coupling an advanced land surface–hydrology model with the Penn state–NCAR MM5 modeling system. Part II: Preliminary model validation. *Monthly Weather Review*, *129*(4), 587–604. https://doi.org/10.1175/1520-0493(2001)129<0587:CAALSH>2.0.CO;2

Crezee, B., Joos, H., & Wernli, H. (2017). The microphysical building blocks of low-level potential vorticity anomalies in an idealized extratropical cyclone. *Journal of the Atmospheric Sciences*, *74*(5), 1403–1416. https://doi.org/10.1175/JAS-D-16-0260.1

Davis, C. A. (1992). A potential-vorticity diagnosis of the importance of initial structure and condensational heating in observed extratropical cyclogenesis. *Monthly Weather Review*, *120*(11), 2409–2428. https://doi.org/10.1175/1520-0493(1992)120<2409:APVDOT>2.0.CO;2

Fan, Z. (2023). Effects of precipitation latent heating on structure and evolution of northeast China cold vortex: A PV perspective [Dataset]. Zenodo. https://doi.org/10.5281/zenodo.8022823

Fan, Z., Zhu, K., & Xue, M. (2023). Decay processes and statistical characteristics of Continental Northeast China cold vortex from April to September. *Acta Meteorologica Sinica*. https://doi.org/10.11676/qxxb2023.20220171

Gao, J., & Gao, H. (2018). Influence of the northeast cold vortex on flooding in northeast China in summer 2013. *Journal of Meteorological Research*, *32*(2), 172–180. https://doi.org/10.1007/s13351-018-7056-3

Gouget, H., Vaughan, G., Marenco, A., & Smit, H. (2000). Decay of a cut-off low and contribution to stratosphere-troposphere exchange. *Quarterly Journal of the Royal Meteorological Society*, *126*(564), 1117–1141. https://doi.org/10.1002/qj.49712656414

Harvey, B., Methven, J., Sanchez, C., & Schäfler, A. (2020). Diabatic generation of negative potential vorticity and its impact on the North Atlantic jet stream. *Quarterly Journal of the Royal Meteorological Society*, *146*(728), 1477–1497. https://doi.org/10.1002/qj.3747

Haynes, P. H., & McIntyre, M. E. (1990). On the conservation and impermeability theorems for potential vorticity. *Journal of the Atmospheric Sciences*, *47*(16), 2021–2031. https://doi.org/10.1175/1520-0469(1990)047<2021:OTCAIT>2.0.CO;2

Hersbach, H., Bell, B., Berrisford, P., Hirahara, S., Horányi, A., Muñoz-Sabater, J., et al. (2020). The ERA5 global reanalysis. *Quarterly Journal of the Royal Meteorological Society*, *146*(730), 1999–2049. https://doi.org/10.1002/qj.3803

Hoskins, B. J., McIntyre, M. E., & Robertson, A. W. (1985). On the use and significance of isentropic potential vorticity maps. *Quarterly Journal of the Royal Meteorological Society*, *111*(470), 877–946. https://doi.org/10.1002/qj.49711147002

Hsieh, Y.-P. (1949). An investigation of a selected cold vortex over North America. *Journal of the Atmospheric Sciences*, *6*(6), 401–410. https://doi.org/10.1175/1520-0469(1949)006<0401:AIOASC>2.0.CO;2

Hu, K., Lu, R., & Wang, D. (2010). Seasonal climatology of cut-off lows and associated precipitation patterns over Northeast China. *Meteorology and Atmospheric Physics*, *106*(1), 37–48. https://doi.org/10.1007/s00703-009-0049-0

Knippertz, P., & Martin, J. E. (2007). The role of dynamic and diabatic processes in the generation of cut-off lows over Northwest Africa. *Meteorology and Atmospheric Physics*, *96*(1–2), 3–19. https://doi.org/10.1007/s00703-006-0217-4

Lamarque, J.-F., & Hess, P. G. (1994). Cross-tropopause mass exchange and potential vorticity budget in a simulated tropopause folding. *Journal of the Atmospheric Sciences*, *51*(15), 2246–2269. https://doi.org/10.1175/1520-0469(1994)051<2246:CTMEAP>2.0.CO;2

Lim, E.-P., & Simmonds, I. (2002). Explosive cyclone development in the southern hemisphere and a comparison with northern hemisphere events. *Monthly Weather Review*, *130*(9), 2188–2209. https://doi.org/10.1175/1520-0493(2002)130<2188:ECDITS>2.0.CO;2

Mlawer, E. J., Taubman, S. J., Brown, P. D., Iacono, M. J., & Clough, S. A. (1997). Radiative transfer for inhomogeneous atmospheres: RRTM, a validated correlated-k model for the longwave. *Journal of Geophysical Research*, *102*(D14), 16663–16682. https://doi.org/10.1029/97JD00237

Nakanishi, M., & Niino, H. (2004). An improved Mellor–Yamada Level-3 model with condensation physics: Its design and verification. *Boundary-Layer Meteorology*, *112*(1), 1–31. https://doi.org/10.1023/B:BOUN.0000020164.04146.98

Nakanishi, M., & Niino, H. (2006). An improved Mellor–Yamada Level-3 model: Its numerical stability and application to a regional prediction of advection fog. *Boundary-Layer Meteorology*, *119*(2), 397–407. https://doi.org/10.1007/s10546-005-9030-8

Nieto, R., Gimeno, L., de la Torre, L., Ribera, P., Gallego, D., García-Herrera, R., et al. (2005). Climatological features of cutoff low systems in the northern hemisphere. *Journal of Climate*, *18*(16), 3085–3103. https://doi.org/10.1175/JCLI3386.1

Palmén, E. H., & Newton, C. W. (1969). *Atmospheric circulation systems: Their structure and physical interpretation* (Vol. 13). Academic press.

Pang, H., & Fu, G. (2017). Case Study of potential vorticity tower in three explosive cyclones over eastern Asia. *Journal of the Atmospheric Sciences*, *74*(5), 1445–1454. https://doi.org/10.1175/JAS-D-15-0330.1

Porcù, F., Carrassi, A., Medaglia, C. M., Prodi, F., & Mugnai, A. (2007). A study on cut-off low vertical structure and precipitation in the Mediterranean region. *Meteorology and Atmospheric Physics*, *96*(1), 121–140. https://doi.org/10.1007/s00703-006-0224-5

Portmann, R., Crezee, B., Quinting, J., & Wernli, H. (2018). The complex life cycles of two long-lived potential vorticity cut-offs over Europe. *Quarterly Journal of the Royal Meteorological Society*, *144*(712), 701–719. https://doi.org/10.1002/qj.3239

Portmann, R., Sprenger, M., & Wernli, H. (2021). The three-dimensional life cycles of potential vorticity cutoffs: A global and selected regional climatologies in ERA-interim (1979–2018). *Weather and Climate Dynamics*, *2*(2), 507–534. https://doi.org/10.5194/wcd-2-507-2021

Price, J. D., & Vaughan, G. (1993). The potential for stratosphere-troposphere exchange in cut-off-low systems. *Quarterly Journal of the Royal Meteorological Society*, *119*(510), 343–365. https://doi.org/10.1002/qj.49711951007

Rossa, A., Wernli, H., & Davies, H. (2000). Growth and decay of an extra-tropical cyclone's PV-tower. *Meteorology and Atmospheric Physics*, *73*(3), 139–156. https://doi.org/10.1007/s007030050070

Schneider, T., Held, I. M., & Garner, S. T. (2003). Boundary effects in potential vorticity dynamics. *Journal of the Atmospheric Sciences*, *60*(8), 1024–1040. https://doi.org/10.1175/1520-0469(2003)60<1024:BEIPVD>2.0.CO;2

Skamarock, W. C., Klemp, J. B., Dudhia, J., Gill, D. O., Liu, Z., Berner, J., et al. (2019). *A description of the advanced research WRF model version 4* (Vol. 145, p. 145). National Center for Atmospheric Research. https://doi.org/10.5065/1dfh-6p97

Thompson, G., Field, P. R., Rasmussen, R. M., & Hall, W. D. (2008). Explicit forecasts of winter precipitation using an improved bulk microphysics scheme. Part II: Implementation of a new snow parameterization. *Monthly Weather Review*, *136*(12), 5095–5115. https://doi.org/10.1175/2008MWR2387.1

Thompson, G., Rasmussen, R. M., & Manning, K. (2004). Explicit forecasts of winter precipitation using an improved bulk microphysics scheme. Part I: Description and sensitivity analysis. *Monthly Weather Review*, *132*(2), 519–542. https://doi.org/10.1175/1520-0493(2004)132<0519:EFOWPU>2.0.CO;2

Uccellini, L. W., Petersen, R. A., Kocin, P. J., Brill, K. F., & Tuccillo, J. J. (1987). Synergistic interactions between an upper-level jet streak and diabatic processes that influence the development of a low-level jet and a secondary coastal cyclone. *Monthly Weather Review*, *115*(10), 2227–2261. https://doi.org/10.1175/1520-0493(1987)115<2227:SIBAUL>2.0.CO;2

Wang, Y., Wang, T., Yang, P., & Xue, W. (2022). A numerical simulation of the "1907" Kaiyuan tornado weather process in Liaoning, Northeast China. *Atmosphere*, *13*(2), 219. https://doi.org/10.3390/atmos13020219

Wei, P., Xu, X., Xue, M., Zhang, C., Wang, Y., Zhao, K., et al. (2023). On the key dynamical processes supporting the 21.7 Zhengzhou record-breaking hourly rainfall in China. *Advances in Atmospheric Sciences*, *40*(3), 337–349. https://doi.org/10.1007/s00376-022-2061-y

Wernli, H., Dirren, S., Liniger, M. A., & Zillig, M. (2002). Dynamical aspects of the life cycle of the winter storm "Lothar" (24–26 December 1999). *Quarterly Journal of the Royal Meteorological Society*, *128*(580), 405–429. https://doi.org/10.1256/003590002321042036

Whitaker, J. S., Uccellini, L. W., & Brill, K. F. (1988). A model-based diagnostic study of the rapid development phase of the Presidents's Day Cyclone. *Monthly Weather Review*, *116*(11), 2337–2365. https://doi.org/10.1175/1520-0493(1988)116<2337:AMBDSO>2.0.CO;2

Wirth, V. (1995). Diabatic heating in an axisymmetric cut-off cyclone and related stratosphere-troposphere exchange. *Quarterly Journal of the Royal Meteorological Society*, *121*(521), 127–147. https://doi.org/10.1002/qj.49712152107

Wirth, V., Appenzeller, C., & Juckes, M. (1997). Signatures of induced vertical air motion accompanying quasi-horizontal roll-up of stratospheric intrusions. *Monthly Weather Review*, *125*(10), 2504–2519. https://doi.org/10.1175/1520-0493(1997)125<2504:SOIVAM>2.0.CO;2

Xie, Z., Bueh, C., Li-Ren, J., & Shu-Qing, S. (2012). The cold vortex circulation over northeastern China and regional rainstorm events. *Atmospheric and Oceanic Science Letter*, *5*(2), 134–139. https://doi.org/10.1080/16742834.2012.11446979

Xu, X., Li, M., Zhong, S., & Wang, Y. (2023). Impact of parameterized topographic drag on a simulated northeast China cold vortex. *Journal of Geophysical Research: Atmospheres*, *128*(3), e2022JD037664. https://doi.org/10.1029/2022JD037664

Xu, X., Xue, M., Wang, Y., & Huang, H. (2017). Mechanisms of secondary convection within a Mei-Yu frontal mesoscale convective system in eastern China. *Journal of Geophysical Research: Atmospheres*, *122*(1), 47–64. https://doi.org/10.1002/2016JD026017

Zhang, C., Zhang, Q., Wang, Y., & Liang, X. (2008). Climatology of warm season cold vortices in East Asia: 1979–2005. *Meteorology and Atmospheric Physics*, *100*(1), 291–301. https://doi.org/10.1007/s00703-008-0310-y

Zhang, L., & Li, Z. (2009). A summary of research on cold vortex over northeast China (in Chinese). *Climatic and Environmental Research*, *14*(2), 218–228.

Zhao, S., & Sun, J. (2007). Study on cut-off low-pressure systems with floods over northeast Asia. *Meteorology and Atmospheric Physics*, *96*(1), 159–180. https://doi.org/10.1007/s00703-006-0226-3

Zhu, K., Xue, M., Zhou, B., Zhao, K., Sun, Z., Fu, P., et al. (2018). Evaluation of real-time convection-permitting precipitation forecasts in China during the 2013–2014 summer season. *Journal of Geophysical Research: Atmospheres*, *123*(2), 1037–1064. https://doi.org/10.1002/2017JD027445